Jaime Berez<sup>a,\*</sup>, Christopher Saldana<sup>a</sup>

<sup>a</sup>George W. Woodruff School of Mechanical Engineering, Georgia Institute of Technology, 801 Ferst Dr, Atlanta, GA 30318, USA

Email addresses: <u>j.berez@gatech.edu</u> (J. Berez)\*, <u>christopher.saldana@me.gatech.edu</u> (C. Saldana)

#### **Abstract**

The rapid pace of development seen in the metal additive manufacturing (AM) process of laser powder-bed fusion (LPBF) requires in-step advances in processes qualification to enable full-scale adoption. This particularly applies to quantifying how powder feedstock conditions impact end-component quality. This study examines how in-machine 17-4 stainless steel powder feedstocks are affected by prior LPBF processes, and how these effects impact subsequent builds. Examinations of powder morphology, chemistry, flowability, and rheology were conducted to characterize the powder conditions. The resultant effects of powder feedstock condition on produced component quasi-static tensile and high-cycle fatigue properties were analyzed. Fatigue life was analyzed using a reliability modeling approach that enabled a robust statistical comparison of life. Powder characteristics were found to evolve with powder exposure to prior LPBF processes, particularly in the extremes of powder size distribution and measures of bulk flow. No significant effects of these changes on tensile properties were observed. Reliability modeling methods, including the lognormal and Weibull distributions as well as the empirical survival function, are shown to be effective tools for modeling fatigue variability in LPBF manufactured components. Through these tools, fatigue life was found to be invariant with changes in powder condition.

Keywords: Additive manufacturing; laser powder bed fusion; metal powder; fatigue; reliability modeling.

### 1 Introduction

Laser powder bed fusion (LPBF) has emerged as a prominent metal additive manufacturing (AM) process which utilizes powdered metals as the feedstock material. The LPBF process uses a scanning laser to selectively fuse cross sectional slices of the final component from a thin powder layer which has been spread over a previous layer, the process repeating for each slice. This methodology enables LPBF to produce high-value added components with difficult to manufacture geometry, tailored material and microstructural properties, and in some cases, favorable mechanical properties [1], [2]. However, while LPBF offers advantages in idealized conditions, the process is inherently prone to defects such as porosity, highly variable material properties, and geometric imprecision [3]–[5]. As such, the potential advantages cannot be reaped unless an advanced set of process qualification techniques can be implemented to enable adoption in high demand applications [5]–[7].

Qualification techniques applied in recent years are broad in their scope and methods and encompass geometric inspection, materials qualification, and produced component destructive and nondestructive evaluation [3], [5], [8], [9]. Although a large amount of work is focused on process and end-product qualification, the control of the raw material feedstocks used in AM has been receiving heightened attention. Industry leading organizations agree that powder feedstocks need further characterization, standardized quality measures, and improved correspondence to end-component quality [6], [10], [11]. The question arises, how does powder condition affect the LPBF process, and which powder characteristics govern component quality? In this study, multiple LPBF builds were manufactured using powder feedstock of varying conditions. Powder conditions were characterized in parallel with produced component and tensile and fatigue properties to answer these questions.

### 2 Background

Powder feedstock qualification is understood to be critical in the holistic manufacturing workflow of metal AM [6], [10], [11]. Notably, the relation between currently available powder characterization methods and relevant outcomes in metal AM processes is still developing [12], [13]. Thus far, many efforts

<sup>\*</sup>Corresponding author

of powder characterization in AM have been motivated by the practice of powder recycling, which is of interest due to the characteristic low material usage efficiency and high material cost of LPBF [14]. Typically, excess powders not fused during the LPBF process are recovered and sieved to remove large and frequently compositionally variable particles that decrease packing density [15]. Established process controls for acceptance of recycled powder are sparse and un-standardized [16], and as a whole recycling is still not universally adopted [17], [18].

Slotwinksi et al. [19] presented the results of a suite of characterization methods aimed at several recycled powders, including 17-4 stainless steel. No significant changes in elemental content were found, however, a small increase in the amount of retained austenite with the degree of recycling was identified, attributed to the powder's exposure to heat during the LPBF process. Despite sieving between re-uses, there was a gradual increase the 90<sup>th</sup> percentile of particle diameter, attributed to elongated agglomerates formed during the LPBF process that were not filtered out by sieving, a claim supported by other work [20]. The recoating process was found to have preferentially transported large particles across the build area and into the powder collector.

Heiden et al. [21] conducted a thorough study of recycled 316L stainless steel powder. They also observed greater sphericity in virgin powders and an increase in satellites and irregular shapes in recycled powders. Large oxide particles were discovered in the recycled powder as well as on the fracture surfaces of failed tensile specimens. The PSD of sieved powders saw a minor depletion of small particles, and tensile properties of produced components, with the exception of elongation, were found to not be greatly influenced by recycling; a set of observations echoed by other studies [16], [22]–[24]. In other works, flowability and apparent density changes have generally been seen to both increase with degree of recycling [16], [22], [23]. These results were observed in several material systems including titanium, nickel-based, aluminum, and stainless-steel alloys.

Two powder recycling studies [23], [25] observed greater permeability of virgin powders, measured by pressure drop of a gas passed through them, attributed to a higher content of agglomerated particles that reduce packing density, increase cohesivity, and inhibit flow, whereas recycling was seen to remove agglomerates via sieving. In both cases, more free-flowing recycled powders with fewer agglomerates resulted in better end-component mechanical properties, attributed to denser powder beds. Powder recycling cannot be universally expected to produce these results; a case study published by Clayton et al. [26] showed that a high basic flowability energy (BFE) was associated to re-used powders that picked up large and non-spherical byproduct particles from the LPBF process and that sieving did little to address this. Ahmed et. al also found poor flowability of recycled powder for similar reasons [20]. Strondl et al. [24] found that virgin powder packed best and had a lower BFE in an electron beam-PBF application while recycled powder packed better and had a higher BFE in an LPBF application. The precise initial state of the virgin powder and subsequent processing have a significant influence on powder evolution.

Given that various treatments and conditions of powders have been shown to produce unfavorable phases, oxides, and porosity, it is reasonable to suspect that such defects would affect end-component fatigue performance [8], [27], [28]. Even so, studies of fatigue as a function of powder characteristics are limited to-date. Carrion et al. [23] studied powder recycling effects on the tensile and fatigue behavior in LPBF processed Ti-6Al-4V. Reported powder measurements agree with the earlier presented works and show a narrowing of PSD due to a depletion of small particles during recycling. This is correlated to increased flowability but also to a theorized lower powder bed density and commensurate increased part porosity. A humid atmosphere is noted to influence particle agglomeration, lowering flowability. Oxygen pick-up, due to atmosphere exposure, was suspected, and microstructural changes as a result of recycling powders were not found. Specimens produced with virgin and recycled powders showed no noticeable differences in low-cycle fatigue (LCF) but results in high-cycle fatigue (HCF), notably with high scatter, argued for better performance for components manufactured with recycled powder.

Only one work known to the authors has studied fatigue behavior in stainless steels as a function of powder characteristics. Soltani-Tehrani et al. [25] studied fatigue in LPBF manufactured 17-4, heat treated to condition H1025, that was built with virgin and recycled powders in a nitrogen atmosphere. Highly recycled powders exhibited improved flowability and less compressibility due to a reduction in fines and

agglomerate powders. In agreement with Ref. [23], improved fatigue life in specimens manufactured from recycled powders was found. Both studies suggest that flowability improvements as result of narrowed PSD and fewer agglomerates were more important in determining powder bed density than the higher ideal packing density of a wider PSD. It should be noted that other work has found that recycling can introduce large aspherical particles which reduce powder layer density and increase part porosity [20], which would theoretically be a detriment to fatigue.

The vast majority of prior work has compared the fatigue properties of metal AM components as a function of processing history via the comparison of stress-life data, strain-life data, or crack growth models. While these tools provide valuable metrics for design, they do not lend themselves towards robust statistical analyses that can readily differentiate material treatments [29]. This is partly owing to the characteristically large statistical variation seen in fatigue data, which is particularly prevalent in metal AM [8]. Reliability modeling presents an interesting set of techniques that statistically describe a single measure (e.g., fatigue life), under a single set of service conditions (e.g., applied stress, strain), which enables comparison of data sets with robust statistical tools. Wirsching and collaborators have provided a strong description of these methods applied to structural fatigue across multiple works [29]–[31]. Parametric methods used to model fatigue most frequently utilize the lognormal, Weibull, or three parameter Weibull probability distribution functions (PDF) [31]–[33]. These methods have been applied to materials prone to defects, e.g. castings or composites [34]–[36], and in areas where cost of failure is high [36]; descriptors which apply to metal AM. Applications in AM have been limited thus far, but include some prior works that successfully modeled variability [37]–[39], but with limited applications that compared material treatments, such as powder condition.

Linking powder properties to produced component properties remains a challenge for the field. Many studies either strictly evaluated powder or assessed mechanical and microstructural properties of produced components, but both tasks have been performed in parallel infrequently. A small number of works spread over several material systems, many of which have been reviewed thus far, perform the two assessments in parallel and can provide only a few strongly evidenced correlations between powder and parts [16], [21]–[23], [40]–[42]. Further, it should be noted that a somewhat narrow definition of powder conditions, relegated to recycled powders, has generally been investigated and that other powder conditions, such as the in-machine prior process exposed powders in this study, require attention. Although the effects of powder condition on tensile performance in most cases was negligible [16], [21]–[24], it is not well understood how fatigue performance will be affected. Notably, of the small body of work that has examined powder condition effects on fatigue [23], [25], sample sizes were small and statistical methods of comparison were not used – more robust analysis is required. In this work, virgin and prior process exposed powder feedstocks were thoroughly characterized through multiple methods to determine their evolution with respect to prior process exposure. The resultant end-component tensile properties were then compared, in addition to a rigorous statistical assessment of fatigue life.

### 3 Materials and methods

## 3.1 Powder use methodology, virgin powder characteristics

Two broad methods of powder feedstock utilization were contrasted in this work through the study of four distinct builds executed consecutively. Figure 1 displays a schematic of the consecutive build processes. A sufficient amount of powder for the four builds (approximately 80 kg) was decanted directly from the powder manufacturer containers into the LPBF machine hopper. After completion of the first build, the process chamber was opened, the hopper covered to protect the remaining powder supplies from undue contamination, a new build plate installed, and the next build initiated. This was repeated until all four builds were complete. In-machine powder supplies were not supplemented or intentionally altered between builds; feedstock powders remained in the hopper and sieving was not performed. The powder used for the first additive build (A1) was of the virgin condition. In the subsequent three builds (i.e., A2, A3, A4), the powder in the hopper had been exposed to prior LPBF process(es). This introduced the powder to multiple potential channels of alteration due to increased atmosphere exposure, operator handling, and

in-chamber LPBF process conditions. These feedstocks were of the prior process exposed condition, with the  $n^{th}$  build being exposed to (n-1) prior processes.

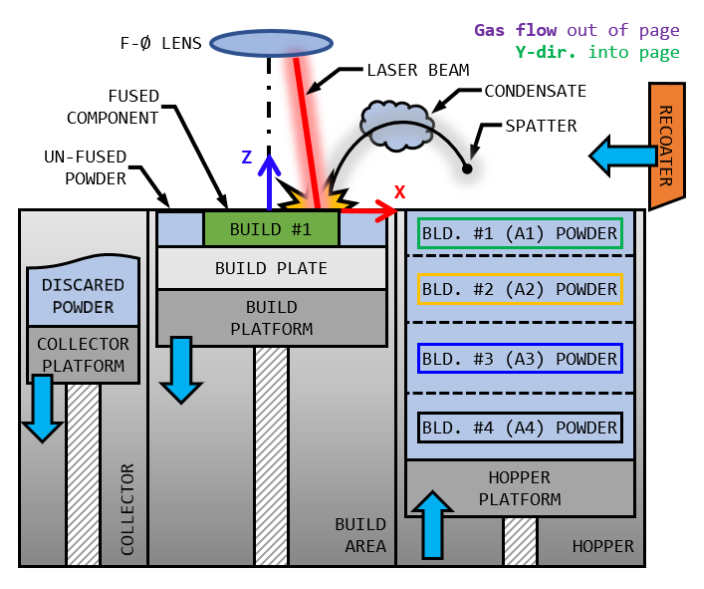


Figure 1. Depiction of the build process. Several methods of powder supply contamination due to the LPBF process are depicted.

This work examines 17-4 stainless steel, a well-known precipitation hardening alloy increasingly used in its powder form for LPBF due to its high strength and corrosion resistant attributes. 17-4, also known as UNS S17400 or AISI type 630, is a compositionally complex stainless steel that is martensitic at service temperatures and primarily strengthened via the precipitation of small Cu-rich particles. The 17-4 powder feedstock used was argon gas-atomized powder, procured from *Praxair Surface Technologies*, under the commercial product name of *Truform 174-161*. The manufacturer lot-specific chemical composition analysis is provided in Table 1 [43]. The manufacturer also reported several other virgin powder characteristics: The powder was reported to have  $d_{10}$ ,  $d_{50}$ , and  $d_{90}$ , parameters of 25, 37, and 55 µm, measured in accordance with ASTM B822. Tap density was reported to be 4.57 g/cm<sup>3</sup>, measured in accordance with ASTM B527. All powder used was from a single lot.

Table 1. Chemical composition of 17-4 virgin powder

obition of i.		PO 11 42				
Elem.	Fe	Cr	Ni	Cu	Mn	Mo
Test result	Bal.	16.27	4.18	3.24	0.03	0.07
Elem.	Si	C	P	S	N	О
Test result	0.76	0.02	< 0.005	0.002	0.007	0.022
Elem.	Sn	Al	Ta	Nb	Other	
Test result	0.00	0.00	0.00	0.19	0.14	

### 3.2 Specimen manufacture

Each build included specimens intended primarily for either uniaxial tensile testing, uniaxial fatigue testing, or microstructural evaluation. Two specimen designs were manufactured for these needs: (1) a universal mechanical test specimen that could be machined to produce tensile or fatigue specimens and (2), a witness specimen. The universal mechanical test specimen was a hexagonal prism, printed horizontally (long axis perpendicular to the build direction), and elevated several millimeters from the build plate by solid supports. The tensile and fatigue specimen as-machined designs, detailed in Figure 2, both had 6.0 mm diameter gage sections, with geometry adherent to ASTM E8 [44] and ASTM E466 [45], respectively.

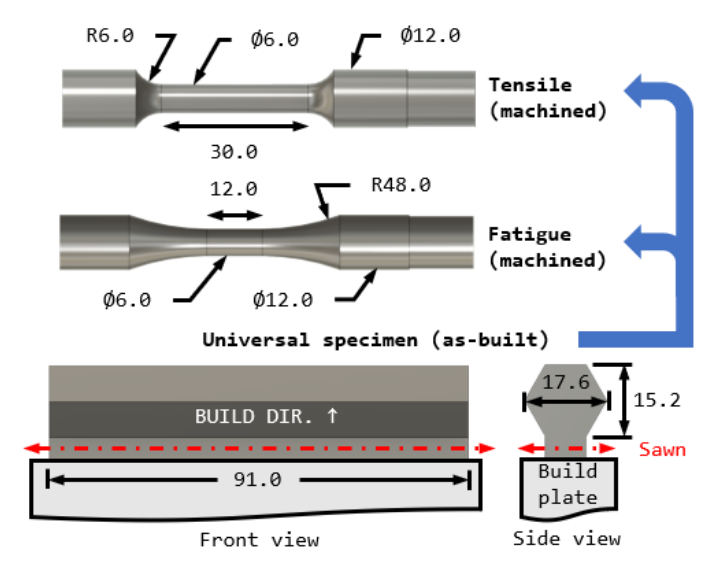


Figure 2. As-machined mechanical test specimen designs and as-built universal specimen. All dimensions are in mm.

An EOS M290 commercial LPBF system was used to manufacture the four consecutive builds. The layout of specimens on a 250 x 250 mm carbon steel build plate is shown in Figure 3. Individual specimens are referred to by their build and location within the build, e.g., specimen A1-2-4 (build A1, row 2, 4<sup>th</sup> position within row 2). Of the 24 mechanical test specimens in each build 10 were selected for tensile testing and 9 for fatigue testing. All four builds were used the same layout, exposure order (also noted in Figure 3), processing parameters, build strategy. Specimens were built using the 'stripes' scan strategy (stripe width = 12 mm) and the 'time homogenization' methodology. The stripes strategy alternates infill scan line orientation by 67° every layer. This strategy, as well as the homogenizing post-build heat treat, make specimen orientation within the X-Y plane non-influential on mechanical properties. Manufacturer provided exposure parameters standard for 17-4, shown in Table 2, were used. Each build process spanned approximately 85 hours.

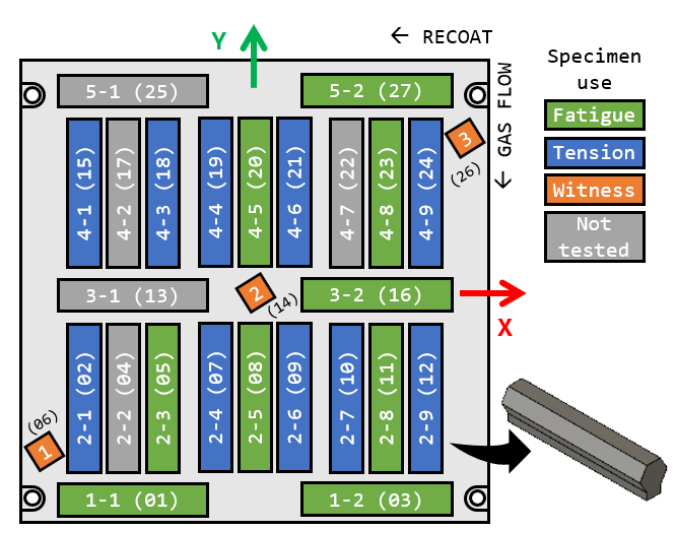


Figure 3. Build layout for all builds. Build direction is +Z, or out of the page. Specimen locations are identified by their two-digit label. Exposure order is noted in parenthesis.

Table 2. LPBF build parameters

Parameter	Value
Layer height	40 μm
Laser power	220 W
Scan speed	755 mm/s
Hatch spacing	0.11 μm
Beam diameter	80 μm
Build plate temperature	80 °C

All specimens from all builds were solutionized and aged in a single lot on the build plates. Per AMS 2759/3 [46], heat treatment to the H1025 condition was accomplished by solutionizing at 1038 °C (1900 °F), quenching in argon to below 32 °C (90 °F), and finally aging at 552 °C (1025 °F) for 4 hours in a vacuum furnace. Quenching was achieved by back-filling with argon. A small amount of 15.9 mm diameter wrought bar (UNS S17400 AISI type 630 specification) was heat treated in the same lot and tested in parallel to provide a baseline of performance. This material is referred to as "Wrt." in subsequent figures.

After heat treatment, all specimens were removed from the build plate by band-sawing and then machined on a CNC turning center to their final geometry. Fatigue specimens were further polished, up to P2000 grit size, to remove tool marks and impart a surface lay parallel to the direction of applied stress. As-machined tensile specimens were inspected with a *Mitutoyo Surftest SJ-410* profilometer and displayed a typical surface roughness of  $R_a = 0.40 \,\mu\text{m}$ , with an upper and lower cutoff of  $\lambda_c = 0.8 \,\text{mm}$  and  $\lambda_s = 2.5 \,\mu\text{m}$ , using a Gaussian filter, according to ASME B46.1. A large sample of polished fatigue specimens were inspected with a *Zygo Zegage* scanning coherence interferometer over an area of 834 x 834 um and found to have average parameters of  $S_a = 0.121$ ,  $S_q = 0.162$ . and  $S_v = -1.300$ , as per ISO 25178 using unfiltered areal data with form removed.  $R_a$  was also measured by extracting a profile perpendicular to the lay and was on average 0.080  $\mu$ m with a standard deviation of 0.023  $\mu$ m, which meets ASTM E466 guidelines.

#### 3.3 Powder characterization

All powder samples were taken from the center of the hopper area immediately prior to each build in accordance with ASTM B215, via practice 1B, using a single-level tube sampler. The virgin powder was sampled directly from the manufacturer container. Samples were immediately stored in sealed containers and kept in an environmentally controlled storage location. For morphological evaluation, powders were placed on carbon tape and imaged using a *Zeiss Ultra 60* SEM operating at an acceleration voltage of 5 kV – all samples were imaged in the same session. PSD was evaluated by laser diffraction techniques according to ASTM B822 using a *Microtrac S-3000* particle size analyzer. Powder light element chemistry was evaluated via combustion and inert gas fusion methods as per ASTM E1019 to detect carbon, nitrogen, oxygen, and sulfur percent content by weight using *LECO CS230* and *LECO TCH600* analyzers.

Powder flow behavior was characterized via Hall flow testing, using "test method 2", as per ASTM B213. A quantity of roughly 50 g (-0.09/+0.16 g) of powder from each of the aforementioned powder samples was used for testing. Each ~50 g sample, one sample per powder condition, was tested three repeated times, and each sample was weighed directly prior to each test. All flow times were taken by a single operator in a single session. A normalized flow time was calculated for each test as  $t_{flow} = t_{meas}*(50/m)$  where the measured flow time ( $t_{meas}$ ) was multiplied by a factor of 50 g divided by the measured mass of the sample (m), also in grams. A *Freeman FT4* powder shear cell was used for rheological evaluation of the powders according to ASTM D7891 – one powder sample from each powder condition was tested. Powders were compacted under a consolidation stress of 6 kPa for testing, which is within a common range for testing of metal powders [23], [24], [26].

#### 3.4 Mechanical testing

Tensile tests were conducted on heat treated and fully machined LPBF manufactured specimens. In addition, a small number of reference tests were conducted on wrought 17-4 bar, heat treated and machined in the same manner. Tests were conducted according to ASTM E8 on an *MTS* servohydraulic 98 kN capacity load frame. Following recommended procedures, specimens were pulled at a strain rate of 0.45 mm/min prior to yield, and 5 mm/min after yield until failure. Once force and strain data were acquired

stress was calculated as the measured force over the nominal cross-sectional area. Yield strength  $(S_y)$  was calculated via the 0.2% offset method and modulus (E) calculated via least-squares fitting of a line to the linear portion of the stress-strain curve. Ultimate strength  $(S_u)$  and elongation at failure  $(\varepsilon_f)$  were extracted as the peak engineering stress experienced and the engineering strain at failure. Ten specimens per build were tested as seen in Figure 3. Specimens from the same locations in each build were used, with the exception of specimen A1-4-1 not being tested and specimen A1-4-7 being tested in its stead.

All tensile data metrics,  $S_y$ ,  $S_u$ , and  $\varepsilon_f$ , were statistically compared between builds with one-way analyses of variance (ANOVA). Each data set was confirmed to be normally distributed, with some deviations at the tails of the data sets. Homogeneity of the respective variances was assessed with Levene's test. In the case of  $S_y$ , Levene's test indicated inhomogeneity, which disagreed with Bartlett's test, leading to an inconclusive result. Elongation was inhomogeneous, likely owing to the relatively small sample size and large number of outlier data typical to this tensile metric.

Fatigue tests were conducted on H1025 condition fully machined and polished specimens. Force controlled constant amplitude axial fatigue tests were conducted according to ASTM E466 on the same load frame. An 8 Hz sinusoidal forcing function with a stress ratio of R = 0.1 was utilized. All tests were conducted with a maximum stress of  $S_{max} = 876$  MPa, selected based on prior testing to produce failure within the HCF regime. Nine tests per build were conducted on specimens from the same locations in each build, as previously detailed in Figure 3.

## 3.5 Fatigue life reliability analyses

### 3.5.1 Non-parametric analysis

To differentiate fatigue performance of the produced components as a function of powder condition, fatigue life data from builds A1, A2, A3, and A4 were first compared using non-parametric statistical methods. The empirical survival function, also known as the Kaplan-Meier estimator, was used to describe the survival probability, i.e., probability for any one specimen to not have failed by N cycles. This metric was evaluated in a stepwise manner, at each cycle count where a failure occurred, as a function of the number of observed failures at a particular cycle count,  $O_N$ , and the number of test specimens still at-risk when the cycle started,  $R_N$ , as seen in equation (1). This resulted in a non-continuous function analogous to the complement of the cumulative density function. An estimator of variance, Greenwood's formula for variance, was calculated for the survival function, and confidence bounds calculated via the z-distribution, as shown in equations (2) and (3).

$$S(N) = \prod_{i:N,s\in N} \left(1 - \frac{O_N}{R_N}\right) \in [0,1]$$
 (1)

$$Var(S(N)) = S(N)^2 \sum_{i: t_i \le t} \frac{O_N}{R_N(R_N - O_N)}$$
(2)

$$Bounds = z_{\alpha/2} \sqrt{Var(S(N))}$$
 (3)

The log-rank test, also known as the Mantel-Cox test, was used to distinguish the empirical survival curves between two or more groups,  $S_g(N)$ , considering sampling error. The test is structured as summarized below.

*Null:* There is no difference in the survival functions of each group. Under the null assumption, the risk of failure at any cycle count, N, is simply  $O_{0,N}/R_{0,N}$ . Thus, the expected number of failures at each observed failure point in each group,  $E_{g,N}$ , is the product of the number of specimens still at risk of failure and the null risk of failure as this point, as shown by equation (4).

Alternative: At least one group's survival function differs from the others. The observed number of failures for each group at each point of failure,  $O_{g,N}$ , is calculated from the data corresponding to each group. The alternative proposes that  $E_{g,N}$  and  $O_{g,N}$  differ.

Once the expected and actual observed number of failures in for each group,  $E_{g,N}$  and  $O_{g,N}$ , were found they were compared across groups to produce a relevant test statistic that could be related to the chi-squared distribution. For m groups being compared, this statistic was compared to the value of chi-squared distribution with k = m - l degrees of freedom evaluated at the desired probability of type I error,  $\alpha$ , as shown by equation (5).

$$E_{g,N} = R_{g,N} \frac{O_{0,N}}{R_{0,N}} \tag{4}$$

$$X^{2} = \sum_{g} \frac{\left(\sum O_{g,N} - \sum E_{g,N}\right)^{2}}{\sum E_{g,N}}$$
 (5)

### 3.5.2 Parametric analysis

The parametric models used to characterize fatigue were the Weibull and lognormal PDFs. The lognormal PDF is a simple log-transformation of the normal distribution and is described by the log-mean and log-standard deviation,  $\mu$  and  $\sigma$ , seen in equation (6). The Weibull distribution is described by the shape and scale parameters,  $\beta$  and  $\eta$ , seen in equation (7).

$$P(x) = \frac{1}{x\sigma\sqrt{2\pi}}exp\left[-\frac{\ln(x-\mu)^2}{2\sigma^2}\right]$$
 (6)

$$P(x) = \frac{\beta}{\eta} \left(\frac{x}{\eta}\right)^{\beta - 1} exp\left[-\left(\frac{x}{\eta}\right)^{\beta}\right]$$
 (7)

After validating the fitness of both models via an exploratory data analysis (see section 4.3), both distributions were fit to the data via maximum likelihood estimation (MLE). MLE is well established and reviewed in the literature, and is suitable for fitting relatively small data sets with complex and non-linear PDFs [47], [48]. The MLE process integral to *Matlab R2020b* and the *Statistics and Machine Learning Toolbox Version 8.6* was utilized. The likelihood ratio test (LRT) was then applied to all possible pairs of fatigue life data sets (A1-A2, A1-A3, etc.). In each paired comparison the test was structured as summarized below.

*Null:* Both groups come from a single population, described by a restricted model with n parameters,  $\theta_1, \dots \theta_n$ . The null likelihood,  $L_0$ , is the likelihood of the single PDF fit to all data via MLE.

Alternative: Both groups come from a distinct population, each described by n parameters, making for an unrestricted model with m = n + n parameters total,  $\theta_1, \dots \theta_m$ . The alternative likelihood,  $L_I$ , is the sum of the likelihoods for the two PDFs that were fit to each data set via MLE.

The likelihood ratio is simply  $\lambda = L_0/L_1$ . By taking the natural log of the ratio and doubling it, as seen in equation (8), a relevant test statistic was produced that follows the chi-squared distribution when the null applies. The test statistic was then compared to a chi-squared distribution at the desired significance level  $\alpha$ , with k = m - n degrees of freedom.

$$X^{2} = -2\ln(\lambda) = -2\ln\frac{L_{0}}{L_{1}} = -2(\ln L_{0} - \ln L_{1})$$
(8)

#### 4 Results & Discussion

#### 4.1 Powder measurements

Powder morphology was qualitatively assessed by the SEM micrographs attained of the various powder samples. Powder samples A2, A3, and A4 all had visually indistinguishable morphological characteristics and, as such, Figure 4a-b display powder used to manufacture build A1 (directly-used virgin) compared to Figure 4c-d which show the powder used to manufacture build A3 (two prior process exposures), sampled from the hopper directly prior to executing each build.

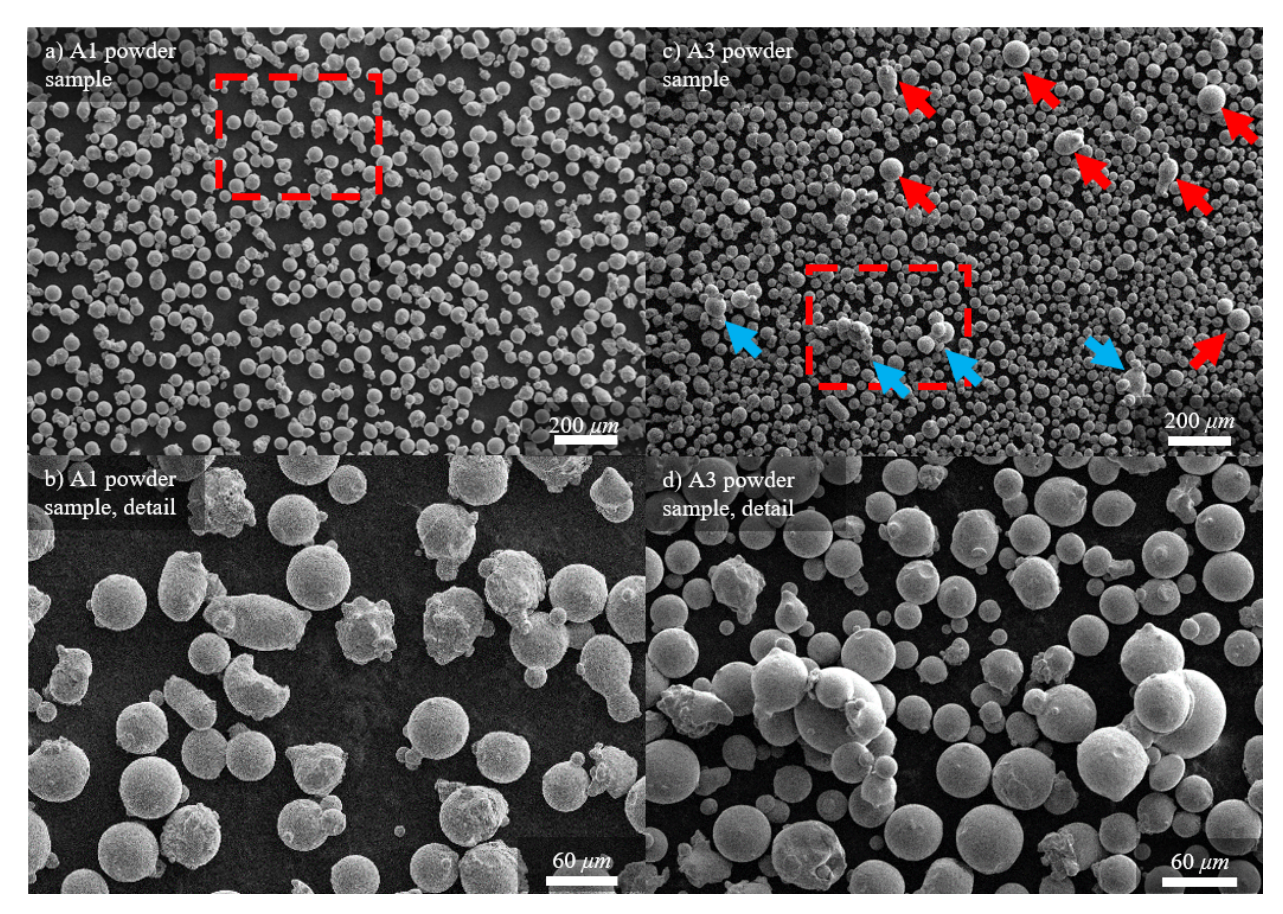


Figure 4. SEM images of powder samples corresponding to the (a)-(b) first (A1) and (b)-(c) third (A3) builds. Suspected spatter particles are identified by red arrows. Particles that display satellites or fusion to other particles suspected as a result of the fusion or spatter process are identified by blue arrows.

The A1 powder sample exhibited particles of a tight size distribution, particularly with a lack of many particles far above 40-50  $\mu m$  in diameter. For reference, the  $d_{90}$  measurement provided by the powder manufacturer was 55  $\mu m$ . There does not appear to be an excess of fine particles either. Particles displayed a morphology typical of the gas atomization process which was used to manufacture the powder [19], [21], [22]. Particles were generally spherical, with a significant proportion accompanied by small satellites. The A3 powder sample notably differed in its make-up due to the presence of very large single particles and large multi-particle satellite formations. These formations were larger and had more particles than those seen in the virgin powder. The large single particles appear to be spatter, from the LPBF process, a claim echoed by other works [20], [49]. The large satellite formations appear to show very smooth surface texture of at least one large particle, indicating that liquid spatter fused with other particles. This form of spatter, referred to by Young et. al. as agglomeration spatter [50], is the most commonly seen form of spatter observed in the SEM micrographs. The particles have been evidently transported to the hopper area via one of several possible mechanisms. Massive, high velocity spatter may have traveled against the dominant shielding gas flow direction or turbulent gas flow in regions of the build area may have been responsible, both suggested in other works [51], [52]. The recoater blade may have also transported them back into the hopper, as particles much larger than the layer height (40 µm) may have been caught on the recoater blade and shed in the hopper during a subsequent recoat. Large, aspherical particles, such as these large satellite formations, can inhibit flow as well as reduce packing density in a spread layer [20], [23], [25], [53].

PSD analysis by light diffraction revealed trends that support these morphology observations. Notably, the PSD mostly experienced changes in the tails, evidenced by a steady  $d_{50}$ , but  $d_{10}$  and  $d_{90}$  measurements that rose by 1.5 and 2.0  $\mu$ m, respectively. The increase in  $d_{90}$  captures the addition of large single spatter particles as well as the formation of the large satellite formations. Note that these percentiles correspond to

the volume distribution, i.e., percentiles by mass, assuming all particles have the same density. The various measures of the PSD mean are more sensitive to the addition of large process byproducts. Particularly, the mean diameter of the number distribution, which was calculated from the reported volume distribution, rose by the greatest value across the four builds,  $5.5 \mu m$ . This metric corresponds to the mean of the distribution that bins particles by diameter according to their frequency. The mean diameter by volume and area each rose by  $3.5 \mu m$ , respectively.

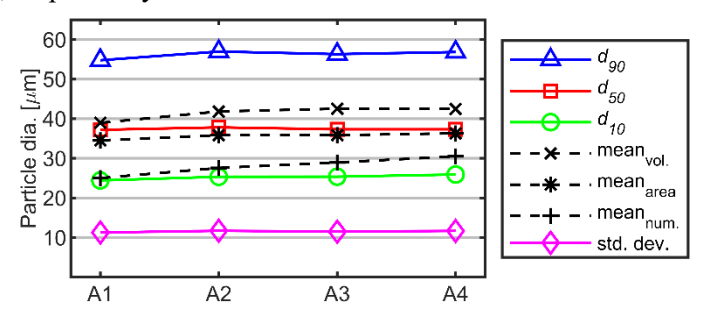


Figure 5. PSD characteristics attained by laser diffraction.

These results are particularly interesting, as the volume distribution is most greatly affected by the presence of large particles, while the number distribution, which experienced the greatest change, is more sensitive to the presence of small particles. Evidently, while SEM imaging of the powders has revealed the new large process byproduct particles, these metrics also suggest small particles depleting with the degree of prior process exposure. Further insight can be had by noting the divergence of  $d_{50}$ , which is the median of the volume distribution, and the mean by volume across the four builds. This shows that the PSD gradually became more right skewed, again indicating new, large particles. All metrics showed the greatest differences between the feedstocks for builds A1 and A2, with less extreme differences in powder samples A2, A3, and A4. Further explanation of this tendency is provided later in this section.

Light element chemistry analysis of the sampled powders is presented in Figure 6. Sulfur content was found not to be in excess of 0.005 % content by weight, the minimum level detectable by the instrument. It appears that exposure to atmosphere and LPBF process conditions minorly affected particle oxygen content, which increased by less than 0.01% content between samples A1 and A2 and stayed above initial levels in subsequent samples. This may be due an increased number of oxidized spatter particles present in the prior process exposed feedstocks. Carbon content, which can significantly affect alloy hardness and microstructure, increased between each powder sample, but only by remarkably small amounts well within the chemistry limits for the alloy. Nitrogen, an austenite stabilizing element, made up less than 0.002 % of particle chemistry in all samples, and did not show any trends.

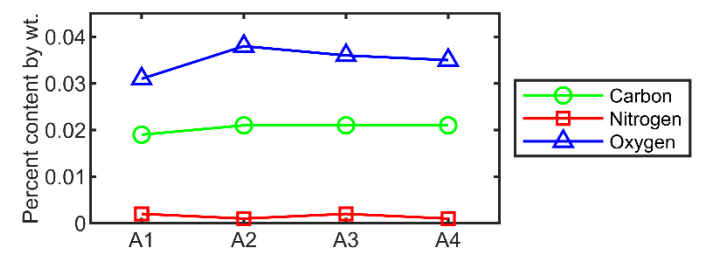


Figure 6. Powder light element chemistry analysis.

Measurements of Hall flowability are presented in Figure 7. The results show an increasing trend in flow time, i.e., a decrease in flowability, accompanying the degree of prior process exposure. This matches BFE measurements from a study that investigated un-sieved re-used powders, which are a similar condition to the prior process exposed powders [26]. A one-way ANOVA with 4 degrees of freedom between groups and 14 degrees of freedom in total was performed on the data, yielding a *F* statistic of 35.7 and a *p*-value of <0.001 as shown in Table 3, resulting in the conclusion that at least one group significantly differed. The data appeared to be distributed normally and Levene's test on the data indicated homogeneity of the

variances. A Tukey-Kramer analysis was performed to further investigate the differences, also shown in Table 3.

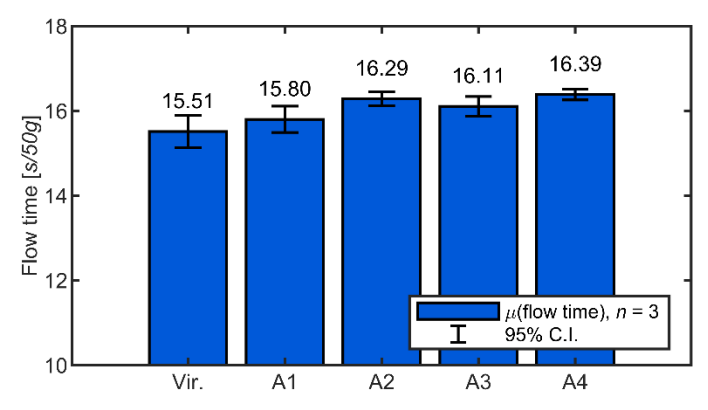


Figure 7. Hall flowability, measured in seconds of flow per 50g sample. The average of three tests with an identical powder sample is presented. 95% confidence intervals are calculated via the relevant t-statistic multiplied by standard error.

The virgin powder displayed a significantly different flowability compared to all other samples. This is interesting for the Vir.-A1 comparison, as the A1 powder is merely sampled from the machine hopper after loading the virgin powder, which was sampled from the powder container. The difference is likely due to a brief but intense to exposure to atmosphere during powder loading and vigorous compaction the powder in the hopper, a standard operating procedure. The A1 powder sample also differed significantly from all other samples. This implies that just one single prior process exposure (i.e., A1 prior to A2) is sufficient to alter the powder supplies in the hopper, and that the effect saturates after a single prior process exposure (i.e., minimal differences between A2, A3, and A4). This is possibly explained by considering the primary method of powder supplies alteration that could inhibit flow – the addition of large spatter particles with satellites, as indicated by the SEM micrographs of Figure 4. Since the recoating process clears off the top layer of powder in the hopper during each recoat, it is likely the case that this mechanism of contamination is consistent regardless of the degree of prior process exposure. The  $d_{90}$  and PSD volume mean trends, seen in Figure 5, show the greatest increases between builds A1 and A2, and provide further convincing evidence of this theory. The increase in particle oxygen content between these two builds would also be explained by this mechanism, which adds spatter particles, known to have high oxide content [21].

Table 3. ANOVA and Tukey-Kramer analysis, tflow

Trainer analysis, then							
	ANOVA						
F		35.7					
p		< 0.001					
Tukey-Kramer analysis							
Comp.	$\Delta_{ m means}$ [sec]	p					
VirA1	-0.29	0.04					
VirA2	-0.77	< 0.001					
VirA3	-0.59	< 0.001					
VirA4	-0.87	< 0.001					
A1-A2	-0.49	< 0.001					
A1-A3	-0.31	0.03					
A1-A4	-0.59	< 0.001					
A2-A3	0.18	0.29					
A2-A4	-0.10	0.77					
A3-A4	-0.28	0.05					
VirA1	-0.29	0.04					

Powder rheometry was investigated via the FT4 powder rheometry testing method. The results of testing virgin powder and feedstocks used to manufacture builds A1, A2, A3, and A4 are presented in Figure 8. The shear stress curves do not imply any differences between the rheological properties of any powder sample, evidenced by the minimal differences between individual gathered data points and overlapping of the curves in multiple places. The reader is referred to other works, [18], [20], [28], which

provide examples of more clearly differentiated powder shear properties. Further analysis of rheological properties can be performed via linear fitting of the data and the construction of several Mohr's stress circle elements, which define characteristics such as cohesivity [54]. Use of these methods here would provide limited analytical utility, as the curves are too poorly distinguished to derive linear trends and Mohr's circle elements with meaningful differences. As such, it was concluded that the rheological shear test did not indicate any detectable differences in the powders. These results do not necessarily contradict the Hall flowability and particle PSD measurements, as rheological powder properties have been repeatably shown to be distinct from flowability measures [26].

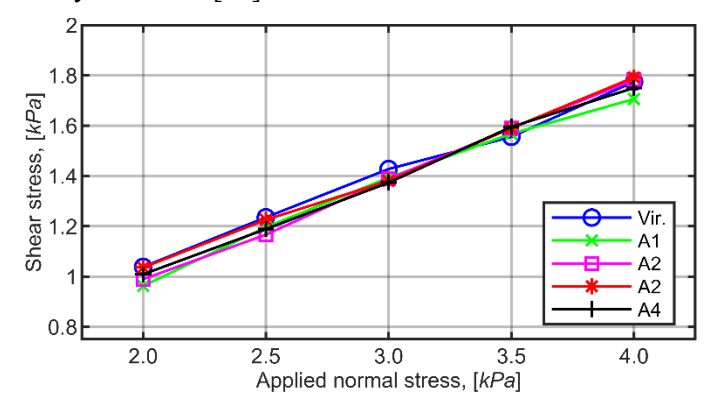


Figure 8. FT4 rheometry test data. Pre-shear data is not pictured.

# 4.2 Quasi-static tensile properties

Tensile tests displayed repeatable stress-strain curves between all additive specimens. Since the curves would effectively overlap each other if all were plotted, one representative curve from each group is shown in Figure 9, along with a curve corresponding to wrought material data. Tensile tests exhibited a stress-strain curve typical of a ductile strain-hardening metal. Necking was exhibited prior to failure and failed specimens showed a classical cup-and-cone structure. The additively manufactured specimens exhibited a lesser degree of strain hardening and lower elongation both of which indicate the absence of large amounts of retained austenite [40], [55], [56]. They also had a higher yield and ultimate strength, all features typical in additive materials partly due to characteristic Hall-Petch strengthening [2], [55].

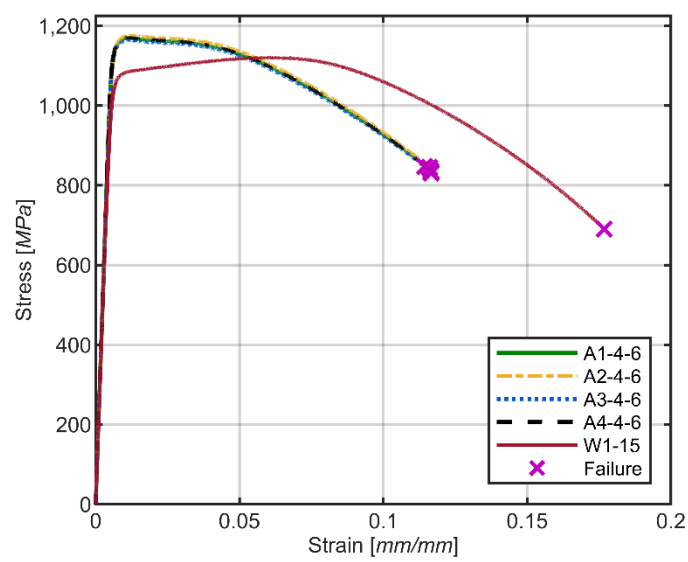


Figure 9. Engineering stress vs. engineering strain for specimens with performance typical of the AM and wrought (W1) groups.

Mean yield strength and ultimate strength data respective to each build are presented in Figure 10. Results from specimen A4-2-6 have been identified as an outlier data point, with no clear explanation.

Exhibited yield was over 4.5 standard deviations lower than the grand mean of all additive tensile tests. Strain data acquisition issues with specimen A1-2-4 prevented extraction of tensile property values. As such, these two specimens were not included in any following analyses. The data labeled "All AM" in Figure 10 as well as subsequent figures refers to statistics that summarize the data from all builds, A1, A2, A3, and A4, considered as a single set.

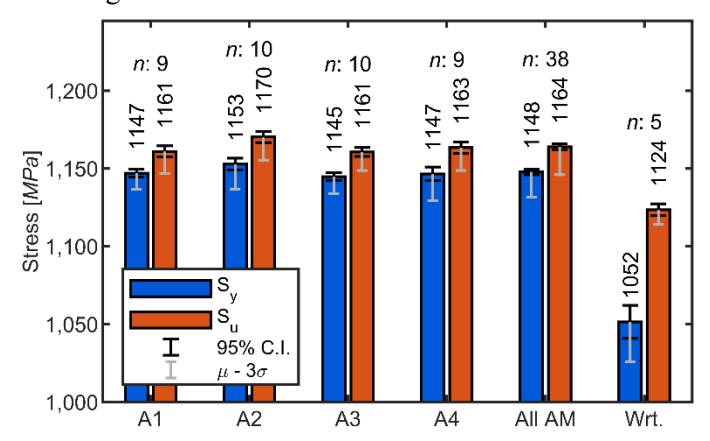


Figure 10. Yield and ultimate strength,  $S_y$  and  $S_u$ , for each group of specimens. 95% confidence intervals are calculated via the relevant t-statistic multiplied by standard error. The mean minus three standard deviations is presented to predict lower-bound performance.

A one-way ANOVA, with 3 degrees of freedom between groups and 37 in total, was utilized to test for differences in both yield and ultimate strengths between groups A1, A2, A3, and A4. The results are summarized in Table 4, and the low p-values indicate with greater than 95% confidence that at least one group differed from the others in both yield an ultimate strength. To further parse these results, a Tukey-Kramer analysis was conducted, also shown in Table 4, which revealed that A2 specimens had significantly greater yield and ultimate strengths compared to all other builds.  $S_y$  and  $S_u$  were higher by less than 10 MPa in all cases, a difference of less than 1%. This is a minor change in these material properties, and without a detailed accounting of the uncertainty budget associated with specimen dimensions, test frame instrumentation, and other sources it is difficult to relegate this result to a systematic material property difference. Additionally, an unknown process variation, such as location within the heat treat furnace, could have introduced this effect. Thus, due to the sole and minor outstanding nature of the A2 specimens and the lack of differences between A1 specimens and any other groups, this is likely not due to a systematic LPBF process variable, nor due to powder condition. Prior work also indicates that powder condition is not expected to greatly affect these tensile properties, which is further discussed later in this section.

Table 4. One-way ANOVA and Tukey-Kramer anlaysis,  $S_v$ ,  $S_u$ , and  $\varepsilon_f$ 

Metric	Yield strength, Sy		Ultimate strength, $S_u$		Elongation at failure, $\varepsilon_f$			
ANOVA								
F	5.64		9.09		2.94			
p	0.003		< 0.001		0.060			
Tukey-Kramer analysis								
Comp.	$\Delta_{\text{means}}$ [MPa]	p	$\Delta_{ m means}$ [MPa]	p	$\Delta_{\text{means}}$ [MPa]	p		
A1-A2	-5.86	0.045	-9.25	0.001	0.03	1.000		
A1-A3	2.18	0.739	0.36	0.998	0.66	0.099		
A1-A4	0.48	0.996	-2.41	0.692	0.04	0.998		
A2-A3	8.04	0.003	9.61	0.000	0.63	0.153		
A2-A4	6.34	0.027	6.85	0.015	0.01	1.000		
A3-A4	-1.70	0.855	-2.76	0.572	-0.62	0.072		

Elongation data are presented in Figure 11. Note that extensometry data past yield was unreliable for a number of specimens from each group, resulting in a smaller number of considered tests (see Figure 11 for the sample size from each build). A one-way ANOVA, with 3 degrees of freedom between groups and 22 in total, is shown in Table 4. The reported *p*-value of 0.060 is of debatable significance. Upon closer

inspection via a Tukey-Kramer comparison, shown in Table 4, this may be attributed to a combination of even less significant differences between groups A1 and A3, as well as groups A2 and A3, with pairwise comparison *p*-values of 0.099 and 0.153, respectively. Due to the high *p*-values of these pairwise comparisons, it is concluded that no significant effects of powder condition on elongation were found.

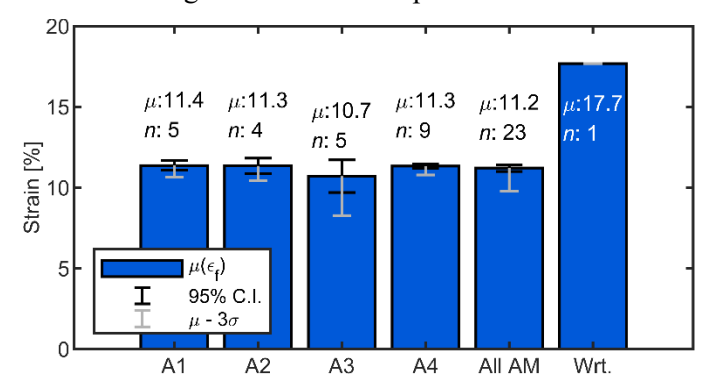


Figure 11. Elongation at failure,  $\varepsilon_b$  for each group of specimens. 95% confidence intervals are calculated via the relevant t-statistic multiplied by standard error. The mean minus three standard deviations is presented to predict lower-bound performance.

Overall, quasi-static tensile metrics do not indicate any component quality differences a function of powder prior process exposure. Other studies have also shown that many tensile properties are robust to several powder reuse conditions [16], [23], albeit with some minor effects on elongation [20]–[22]. It would appear that the prior process exposed powders were less severely altered in their inherent properties and consequently have had no detectable impact on tensile behavior, in any measured metric.

## 4.3 Fatigue properties of produced components

While tensile performance has previously been shown to be somewhat insensitive to powder condition changes, fatigue is more sensitive to the defects that poor powder quality might produce. The processing history of the specimens in this work is expected to create favorable conditions for fatigue performance. Prior work has shown that retained austenite should be largely absent due to the Ar atmosphere used during both powder gas atomization and LPBF processing [55], [57], [58]. Additionally, the solutionizing and aging H1025 heat treatment can be expected to also remove austenite, homogenize the microstructure [59], and produce an alloy with superior fatigue performance relative to the peak-aged and as-built conditions [25], [60], [61]. Further, the machined specimens are without rough as-built surfaces, which otherwise might dominate fatigue behavior [7], [61], [62]. As such, fatigue life should be largely governed by the defect content of each specimen, including those defects attributable to unfavorable powder characteristics. To assess these effects, the fatigue lives of the nine tested specimens from each build are presented in Figure 12 on a logarithmic scale. All tests were conducted at a loading ratio of R = 0.1, and maximum stress of  $S_{max} = 867$  MPa. A significant amount of variation within each group is evident – lives vary from roughly 21,000 to 1,800,000 cycles between all the groups. A visual examination the data does not reveal any readily detected differences.

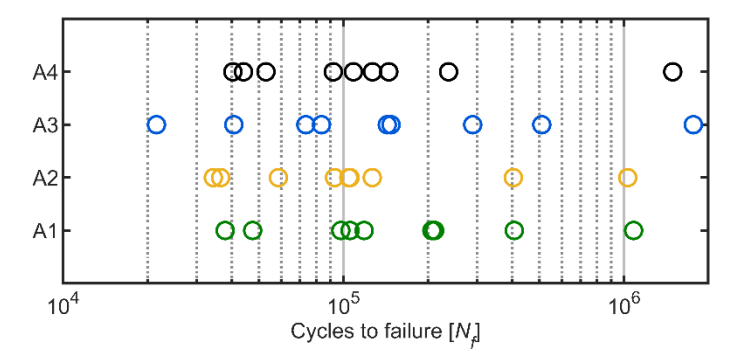


Figure 12. Fatigue life of all specimens tested at S<sub>max</sub> = 867 MPa, R = 0.1. The vertical axis organized data by build (A1, A2, A3, A4).

In order to better distinguish the data, the empirical survival function was calculated for each group. This non-parametric approach is of interest as it does not rely on fitting of deterministic models to data and is thus useful in cases where a data set is small or cannot be confidently said to adhere to a known model. Results are presented in Figure 13a, where the probability of survival past N cycles is presented as a function of N (plotted on a logarithmic scale). Greenwood's formula for variance was used to calculate confidence bounds on the functions for groups A1 and A4, shown in Figure 13b. Neither figure suggests differences between the groups. The confidence bounds in Figure 13b overlap considerably.

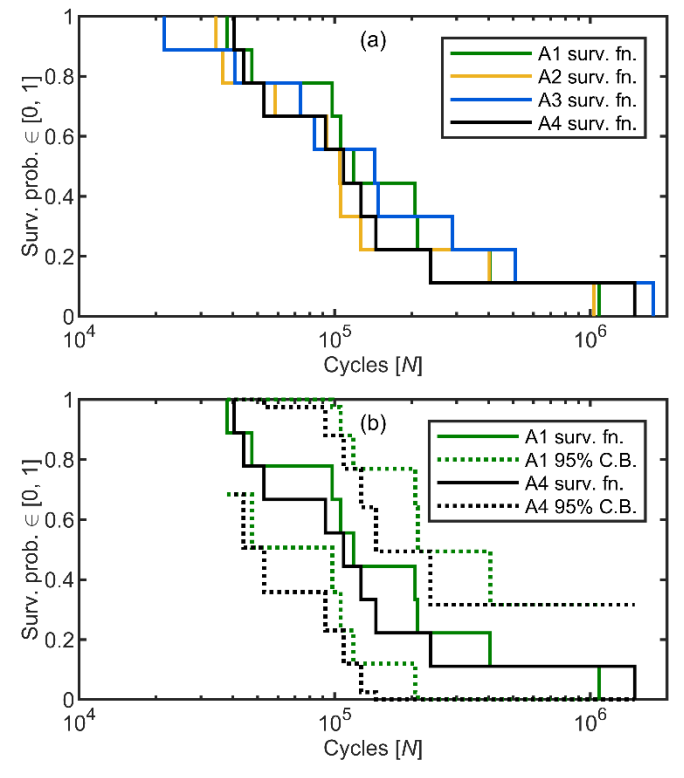


Figure 13. (a) Empirical survival functions for specimens tested at  $S_{max} = 867$  MPa, R = 0.1. (b) Empirical survival functions for groups A1, and A4. 95% confidence bounds are derived by Greenwood's formula.

The log-rank test was applied to further compare the respective survival functions. The log-rank test handles right-skewed distributions well and, although censoring was not necessary with this data set, can account for censored data. Additionally, the test can consider more than two groups, increasing the power of the test, as opposed to multiple pairwise tests. The significance level used for this test was  $\alpha = 0.10$ , which was used in combination with k = 3 degrees of freedom to calculate the critical test statistic value of  $X^2_{crit} = 6.25$ . All four tests were considered simultaneously, and the log-rank test showed no significant difference between the groups, with the test statistic calculated to be X = 0.91 and a p-value of 0.82.

To facilitate a parametric analysis of fatigue life, which is dependent on fitting deterministic models to the data, an exploratory data analysis was first conducted to choose the appropriate descriptive models. Figure 14a-e display the data on probability plots corresponding to normal, exponential, extreme value, lognormal, Weibull, and three-parameter Weibull PDFs. All four groups were considered simultaneously for the sake of choosing a common underlying model. These plots utilize non-linear vertical axes specific to the distribution type that would arrange data linearly should the distribution be a perfect model for the data – deviation from linearity indicates a poor model fit. The dashed line drawn on the plots presents a crude linear judge, connecting the 25<sup>th</sup> and 75<sup>th</sup> percentiles of the data.

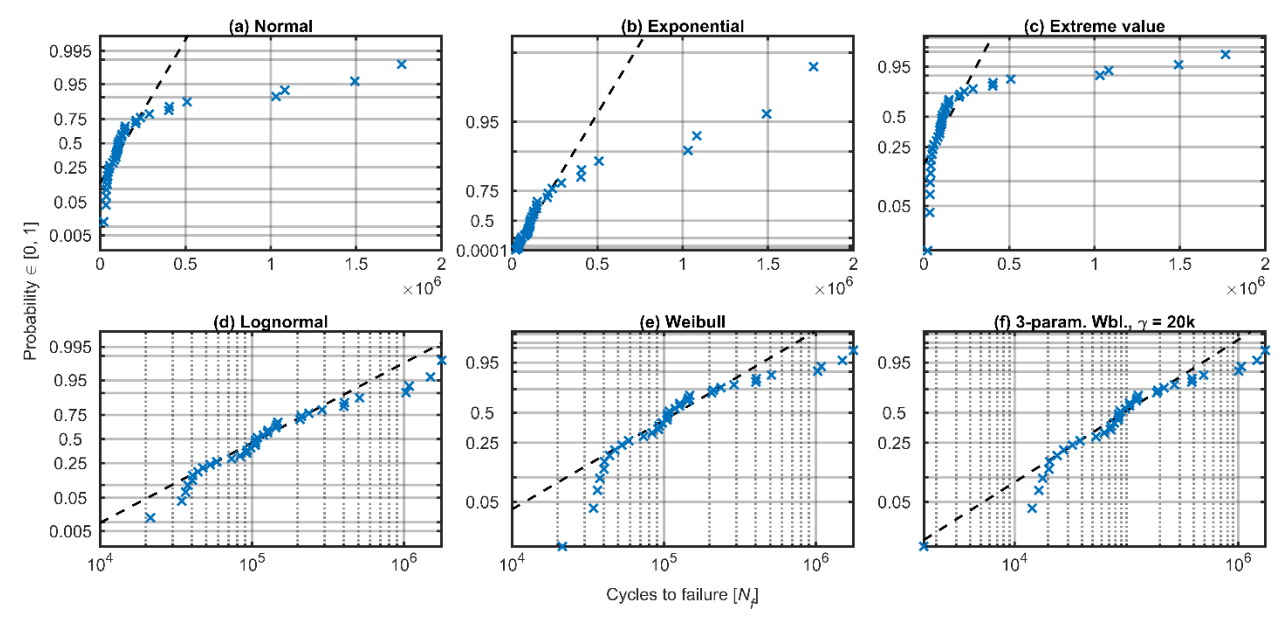


Figure 14. Probability plots of six distribution types (labeled) using the life data for tests conducted at  $S_{max} = 867$  MPa and R = 0.1. Life,  $N_f$ , is on the horizontal axes, probability of failure,  $P(N_f) \in [0, 1]$ , is on the vertical axes. The lognormal and Weibull plots use logarithmic horizontal axes.

The normal and extreme value distributions have significant weaknesses with modeling life at both tails. The exponential distribution shows some promise, but it is a reduction of the more complex Weibull distribution and has weaknesses in modeling long lives. The lognormal and Weibull distributions show the data fairly linearly, distribute the data evenly, and provide a fairly accurate model for specimens that displayed a lower life – an important aspect since these specimens provide a lower bound to performance. Both distributions can be right-skewed, which accurately describes fatigue as a phenomenon with a lower limit and infrequent instances of atypically long lives. Given these attributes and the historical basis for modeling fatigue data with Weibull and lognormal distributions, both distributions were selected for further analysis.

One weakness of the two down-selected distributions is that neither has a non-zero definite lower bound, meaning data with a value of  $N_f = 0$  has a finite probability of occurring. The three-parameter Weibull distribution, described by equation (9), attempts to account for this by shifting the distribution by a constant value,  $\gamma$ . This was chosen to be  $\gamma = 20,000$  cycles, which was subtracted from the data set, then plotted on a Weibull probability plot as shown in Figure 14f.

$$P(x) = \frac{\beta}{\eta} \left( \frac{x - \gamma}{\eta} \right)^{\beta - 1} exp \left[ -\left( \frac{x - \gamma}{\eta} \right)^{\beta} \right]$$
 (9)

While this resulted in the data appearing marginally more linear than the simpler two-parameter Weibull plot, the extra degree of freedom in parameterization of the distribution would obfuscate MLE methods for fitting and also make comparisons of models more complex. As such, the three parameter Weibull distribution was excluded from further in favor of the simpler Weibull distribution.

To compare fatigue life between groups, lognormal and Weibull distributions were fit to each of the four sets of data via MLE. The outcome was parameter estimations for each distribution, in addition to asymmetric confidence intervals based on the sample size and variability of the data, displayed in Figure 15. Group A1 displayed both the highest log-mean and lowest log-standard deviation. It also had highest shape parameter in the case of the Weibull models. This indicates that specimens from build A1 had a slightly right-shifted life probability distribution. Interestingly, the relative differences between groups in the log-mean (lognormal) and scale (Weibull) parameters followed the same trends. Both parameters are measures of central tendency, and the same relative trends imply that both distribution types identify the same overall tendencies in the data. The shape parameters indicate that the PDF shape proceeded from bell-shaped to exponential across the builds, but only minimally so. The large overlap of the confidence intervals

for all parameters of both distribution types argues for a lack of significant model differences at this stage of analysis.

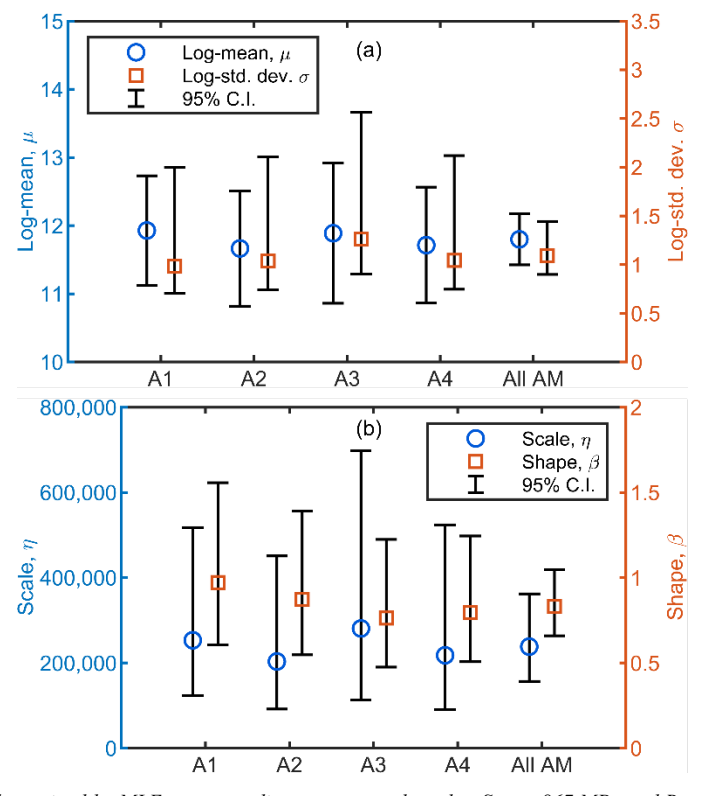


Figure 15. Model parameters determined by MLE corresponding to tests conducted at  $S_{max} = 867$  MPa and R = 0.1. (a) Lognormal parameters. (b) Weibull parameters.

The likelihood ratio test (LRT) was used with the MLE fitted distributions to produce a definitive comparison between the groups. The LRT can only be utilized for comparisons between two models at a time, so six pair-wise comparisons were performed, as seen in Table 5. The test statistic,  $-2 \ln(\lambda)$ , was compared to the chi-squared distribution with k=2 degrees of freedom for all comparisons. The significance level used for this test was  $\alpha=0.10$ , which was used to calculate the critical test statistic value of  $X^2_{crit}=4.61$ . None of the comparisons produced a test statistic that met the chosen significance level, indicating no detectable differences in the distributions of fatigue lives. Comparisons to A3 showed the greatest group-to-group differences when using either a lognormal of Weibull model, but the p-values were too high to suggest any significant differences. Interestingly, the likelihood ratio tests using the lognormal and Weibull distributions both resulted in p-values with similar relations between group-to-group comparisons, indicating again that both distribution types can be relied on to provide analogous comparisons.

Table 5. Likelihood ratio test results

	Lognormal est.			Weibull est.		
Comparison	$X^2$	Нур.	р	$X^2$	Нур.	р
A1-A2	0.20	Null	0.906	0.24	Null	0.888
A1-A3	0.69	Null	0.710	0.47	Null	0.791
A1-A4	0.37	Null	0.832	0.14	Null	0.932
A2-A3	0.63	Null	0.729	0.42	Null	0.811
A2-A4	0.13	Null	0.937	0.08	Null	0.960
A3-A4	0.23	Null	0.892	0.33	Null	0.846

As is evident, fatigue life is a highly stochastic property, typically seen to exhibit coefficients of variation of 25-75% [30], [63], but in this case exhibiting a coefficient of variation in excess of 150%. Other authors have identified AM process-induced defects to be particularly responsible for very high degrees of

scatter [8]. Despite the large range of life displayed in this work, fracture surfaces displayed largely consistent characteristics. The fracture surface of a representative fatigue specimen is shown in the optical micrograph of Figure 16a. A fracture growth region normal to the direction of stress is clear, surrounded by shear lips created by gross ductile final failure. Figure 16b shows an SEM micrograph of the fracture growth region of specimen A2-1-1, with chevrons pointing towards a single initiation site, located near the surface, as was the case with nearly all specimens. The initiation site, seen in detail in Figure 16c, is a lack-of-fusion (LoF) defect approximately 80 µm in its largest apparent dimension. It is identified by both the dendritic surface texture that implies the solidification of a free surface and the unmelted powder particle present within the LoF defect area.

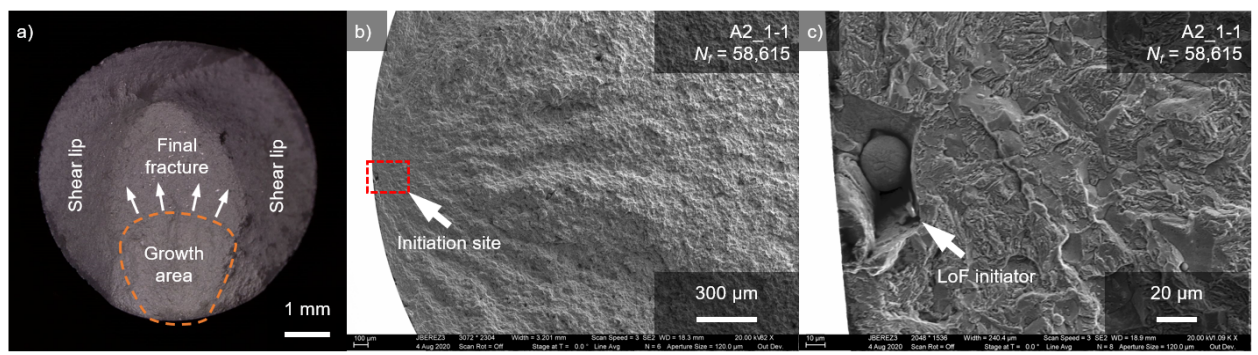


Figure 16. (a) Optical fractograph of a representative fracture surface. The brittle fracture growth area is outlined in dotted orange. (b) SEM fractograph of a fracture growth region, specimen A2-1-1 (Nf = 58,615). The boxed area in red is presented in (b), a detail view of the LoF initiator.

Further fractography showed that a vast majority of specimen fracture initiators appear to be LoF defects, consistent with other results [25], [64]. Figure 17 shows fractographs depicting initiation sites from specimens belonging to each build, i.e., attributable to each powder condition. Each specimen displayed relatively low life, 50,000 cycles or less. In all cases, a large LoF defect, ranging from 80 to 160 µm in its largest apparent dimension, was identified as the fracture initiating defect. As is evident, the low-performing specimens of each build showed similar mechanisms that led to premature failure.

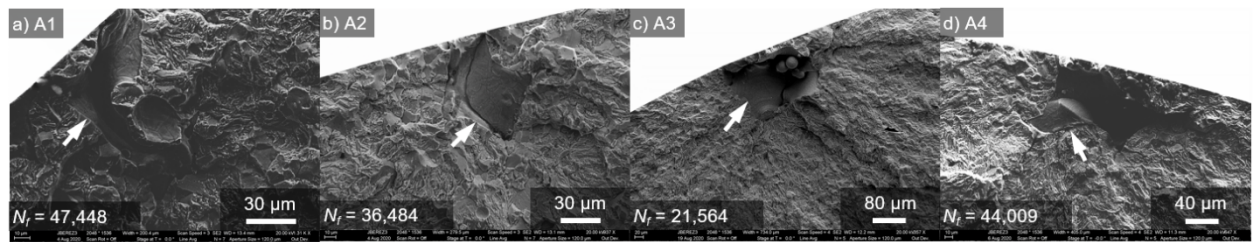


Figure 17. Selected fractographs. White arrows identify the LoF defect.

A logical line can be drawn between powder condition and end-component defects seen in Figures 16 and 17 – should a powder have poor flowability or contain large aspherical particles which lower the local powder layer packing density, this may form pre-fusion voids in the powder bed which cannot be sufficiently bridged by a relatively small meltpool. The prior process exposed powders, display these qualities which could have had such an effect, but the statistical analysis of fatigue data presented thus far proves they did not. One explanation for this would be that the unfavorable properties of the prior process exposed powders are not a dominant mechanism that controls powder bed quality and component defects. It is possible that other process mechanisms may produce the majority of LoF defects, and that these mechanisms would have to be assuaged before prior process exposed powder conditions would drive systematic LoF defect creation.

Prior work has also examined fatigue and porosity as a function of powder properties in LPBF. Ref. [23] and Ref. [25] found that sieving used powders led to improved measures of quality, whereas Ref. [20] found that recycled powder quality degraded despite sieving used powder. The sieve size in all studies was similar (75-80 µm). Importantly, in all cases, the understanding of which powder measures (e.g., narrow

PSD, few large agglomerates, good flowability) produce good part quality (e.g., improved HCF life [23], [25], lowered part porosity [20]) was congruent. However, sieving used powder was seen to improve powder quality in only some cases. The resulting practitioner wisdom is this: the precise characteristics of supplied virgin powders alter the effects of powder recycling. Sieving does not serve to only remove spatter and other LPBF process byproducts; in Ref. [23] and [25] it appeared to improve on virgin powder characteristics regardless of feedstock contamination by the LPBF process. However, if initial virgin powder quality is high, the effect of LPBF process byproducts on powder quality is more important, and the effectiveness of the sieving process used to address this plays a bigger role.

In the present work, the in-machine feedstocks were found to be contaminated by environmental exposure and spatter, which could lower powder quality (e.g., additional large particles, inhibited flowability, minor oxygen pick-up), in a similar manner as has been seen in prior work. Despite this, an exhaustive statistical analysis of fatigue life using relative high sample sizes did not find any differences in fatigue performance associated with powder condition. This observation is explained by two main factors. First, the precise nature of prior process exposed powders as opposed the above-mentioned recycled powders should be considered. Exposure of in-machine feedstocks to atmosphere can be considered to potentially have cumulative effects – more prior processes lead to longer and more significant exposures. That said, particle chemistry and bulk behavior measurements do not show cumulative trends, likely due to the prior process exposed feedstocks in the hopper being reasonably protected from atmosphere due to their dense packing and fastidious operator behavior. In contrast to the environmental exposure method of powder alteration, LPBF process byproducts appear to impact in-machine feedstocks in a non-cumulative manner independent of the degree of prior process exposure, as evidenced by PSD and Hall flow trends. Again, since the powder is packed into the hopper, only the top layer is easily contaminated during the LPBF process. As a result, alteration of in-machine feedstocks likely occurs quickly during the LPBF process and appears to saturate in its effect between subsequent builds. Recycled powders, on the other hand, are cumulatively impacted between distinct builds by either the sieving process (not used here) or the cumulative pick-up of LPBF process byproducts over many builds. Simply put, the changes seen in prior process exposed powders are both distinct and minor compared to previously reported results.

Secondly, as already alluded to, the invariant fatigue life between builds, but with noted high variability in life, suggests that defect-causing process mechanisms independent of the feedstock quality measures drove fatigue performance. Further investigation into these mechanisms might explain the high variability in the fatigue data and inform how to improve material performance from a manufacturing process perspective. It is possible that if powder feedstocks in the hopper can be contaminated by LPBF process byproducts, the powder bed in the build area could be similarly affected. The distribution of spatter particles within each layer may locally alter powder bed quality and be a significant driver of produced component performance.

#### 5 Conclusions

In this work, an understudied powder condition, prior process exposed powder, was characterized and shown to change with the degree of prior process exposure albeit with limited effects on the end-product. The feedstock material used in LPBF should not be thought of as static in its attributes once loaded into a machine, as it evolves with exposure to processing conditions. The reliability modeling methods used effectively established the relative similarity of the fatigue lives attributed to different powder conditions and, prior to the present study, have had limited usage in understanding fatigue in metal AM. Critically, high cycle fatigue life showed a degree of tolerance for changes in powder feedstock size distribution and flowability, which should encourage the use of prior processed exposed powders. An enumeration of the conclusions drawn from this study are presented below.

1. Prior process exposed in-machine powder supplies evolved quickly, with less than 85 hours of build time significantly altering A2 powder supplies. Subsequent process exposures minorly altered the A3 and A4 powder supplies. Fusion process byproducts increased the number of large particles and satellite formations, which also appears to have reduced flowability. PSD metrics of the particle size frequency

- distribution were more sensitive to these changes than the  $d_{10}$ ,  $d_{50}$ , and  $d_{90}$  metrics based on the particle size volume distribution. Powder chemistry and rheology were largely insensitive to prior process exposure.
- 2. The evolution of in-machine powder supplies due to prior process exposure produced a unique powder condition unlike the condition of recycled powder. Recycling has often been shown to produce the opposite trends in flowability, and sieving practices effectively limit the presence of large particles at PSD extremes, unlike in the case of prior process exposed powder.
- 3. The in-machine prior process exposed powders did not produce detectable effects in quasi-static tensile properties of yield strength, ultimate strength, elongation, or modulus.
- 4. High cycle fatigue life was invariant with powder feedstock condition. Both the lognormal and Weibull distributions appropriately modeled the fatigue data. The log-rank and likelihood ratio tests that compared the non-parametric survival functions and parametric lognormal and Weibull fit PDFs detected no differences in fatigue life due to powder condition.
- 5. A rigorous comparison of fatigue life was enabled by a reliability modeling approach and associated statistical tests. A simple comparison of stress-life or strain-life curves with a similarly sized data set would have been frustrated by the high variability associated with AM materials, and suffered from the limited statistical tools available to compare these curves.
- 6. The fatigue life of the LPBF specimens was highly right-skewed, and variation was high. Despite powder feedstock changes between builds that might be expected to affect powder spreading and packing behavior, effects were not severe enough alter resultant fatigue performance. Further examination of HCF fatigue associated with this alloy and process is needed to better characterize dominant drivers of defect creation and subsequent fatigue life variation.

### CRediT authorship contribution statement

Jaime Berez: Writing – original draft, writing – review & editing, conceptualization, methodology, investigation, formal analysis, visualization, software, data curation. Christopher Saldana: Writing – review & editing, conceptualization, supervision, project administration, funding acquisition.

## Acknowledgements

This work was supported in part by the Department of Energy [DE-EE0008303]; and the National Science Foundation [CMMI-1825640]. The authors would like to acknowledge the staff of Delta TechOps' additive manufacturing team (Dr. Ramesh Ramakrishnan, Adapa Venkata Surya, Jaikp Mallory, Donnell Crear, and Dr. John Robertson), as well as Dr. James Collins and Dr. Richard Cowan for their technical guidance, and Elliott Jost for his feedback on this manuscript.

#### References

- M. Schmidt et al., "Laser based additive manufacturing in industry and academia," CIRP Annals, vol. 66, no. 2, pp. 561–583, 2017, doi: 10.1016/j.cirp.2017.05.011.
- [2] M. Kamal and G. Rizza, "Design for metal additive manufacturing for aerospace applications," in *Additive Manufacturing for the Aerospace Industry*, Elsevier, 2019, pp. 67–86. doi: 10.1016/B978-0-12-814062-8.00005-4.
- [3] R. K. Leach, D. Bourell, S. Carmignato, A. Donmez, N. Senin, and W. Dewulf, "Geometrical metrology for metal additive manufacturing," CIRP Annals, pp. 1–24, Jun. 2019, doi: 10.1016/j.cirp.2019.05.004.
- [4] E. Stugelmayer, "Characterization of Process Induced Defects in Laser Powder Bed Fusion Processed AlSi10Mg Alloy," Graduate Theses & Non-Theses, Montana Tech, 2018. [Online]. Available: https://digitalcommons.mtech.edu/grad\_rsch/157
- [5] M. Seifi, A. Salem, J. Beuth, O. Harrysson, and J. J. Lewandowski, "Overview of Materials Qualification Needs for Metal Additive Manufacturing," JOM, vol. 68, no. 3, pp. 747–764, Mar. 2016, doi: 10.1007/s11837-015-1810-0.
- [6] D. Bourell, M. C. Leu, and D. W. Rosen, Eds., "Roadmap for Additive Manufacturing, Identifying the Future of Freeform Processing." The University of Texas at Austin, 2009.
- [7] A. Yadollahi, M. J. Mahtabi, A. Khalili, H. R. Doude, and J. C. Newman, "Fatigue life prediction of additively manufactured material: Effects of surface roughness, defect size, and shape," Fatigue Fract Eng Mater Struct, vol. 41, no. 7, pp. 1602–1614, Jul. 2018, doi: 10.1111/ffe.12799.
- [8] A. Yadollahi and N. Shamsaei, "Additive Manufacturing of Fatigue Resistant Materials: Challenges and Opportunities," *International Journal of Fatigue*, vol. 98, pp. 14–31, May 2017, doi: 10.1016/j.ijfatigue.2017.01.001.
- [9] A. du Plessis, I. Yadroitsev, I. Yadroitsava, and S. G. Le Roux, "X-Ray Microcomputed Tomography in Additive Manufacturing: A Review of the Current Technology and Applications," 3D Printing and Additive Manufacturing, vol. 5, no. 3, pp. 227–247, Sep. 2018, doi: 10.1089/3dp.2018.0060.
- [10] Energetics Incporated, Ed., "Measurement Science Roadmap for Metal-Based Additive Manufacturing." NIST, May 2013.

- [11] Atomization Technology Innovation Consortium, Ed., "Roadmap for the Development of Advanced Atomization and Spraying Technologies." ASM International, Mar. 2017.
- [12] D. M. Drake, "Key Quality Characteristics of Metal Powder for Powder Bed Fusion and Directed Energy Deposition," Colorado School of Mines. 2018.
- [13] T. Senthilvelan, K. Raghukandan, and A. Venkatraman, "Testing and Quality Standards for Powder Metallurgy Products," *Materials and Manufacturing Processes*, vol. 18, no. 1, pp. 105–112, Jan. 2003, doi: 10.1081/AMP-120017592.
- [14] M. Barclift, S. Joshi, T. Simpson, and C. Dickman, "Cost Modeling and Depreciation for Reused Powder Feedstocks in Powder Bed Fusion Additive Manufacturing," in *Proceedings of the 26th Annual International Solid Freeform Fabrication Symposium*, Austin, Texas, p. 22.
- [15] J.-P. Kruth, G. Levy, F. Klocke, and T. H. C. Childs, "Consolidation phenomena in laser and powder-bed based layered manufacturing," CIRP Annals, vol. 56, no. 2, pp. 730–759, 2007, doi: 10.1016/j.cirp.2007.10.004.
- [16] G. Jacob, C. U. Brown, M. A. Donmez, S. S. Watson, and J. Slotwinski, "Effects of powder recycling on stainless steel powder and built material properties in metal powder bed fusion processes," National Institute of Standards and Technology, Gaithersburg, MD, NIST AMS 100-6, Feb. 2017. doi: 10.6028/NIST.AMS.100-6.
- [17] J. A. Slotwinski and E. J. Garboczi, "Metrology Needs for Metal Additive Manufacturing Powders," JOM, vol. 67, no. 3, p. 6, 2015, doi: 10.1007/s11837-014-1290-7.
- [18] A. T. Sutton, C. S. Kriewall, M. C. Leu, and J. W. Newkirk, "Powder characterisation techniques and effects of powder characteristics on part properties in powder-bed fusion processes," *Virtual and Physical Prototyping*, vol. 12, no. 1, pp. 3–29, Jan. 2017, doi: 10.1080/17452759.2016.1250605.
- [19] J. A. Slotwinski, E. J. Garboczi, P. E. Stutzman, C. F. Ferraris, S. S. Watson, and M. A. Peltz, "Characterization of Metal Powders Used for Additive Manufacturing," J. RES. NATL. INST. STAN., vol. 119, p. 460, Oct. 2014, doi: 10.6028/jres.119.018.
- [20] F. Ahmed et al., "Study of powder recycling and its effect on printed parts during laser powder-bed fusion of 17-4 PH stainless steel," Journal of Materials Processing Technology, vol. 278, p. 116522, Apr. 2020, doi: 10.1016/j.jmatprotec.2019.116522.
- [21] M. J. Heiden *et al.*, "Evolution of 316L stainless steel feedstock due to laser powder bed fusion process," *Additive Manufacturing*, vol. 25, pp. 84–103, Jan. 2019, doi: 10.1016/j.addma.2018.10.019.
- [22] P. D. Nezhadfar, A. Soltani-Tehrani, A. Sterling, N. Tsolas, and N. Shamsaei, "The Effects of Powder Recycling on the Mechanical Properties of Additively Manufactured 17-4 PH Stainless Steel," presented at the Solid Freeform Fabrication, Austin, Texas, 2018.
- [23] P. E. Carrion, A. Soltani-Tehrani, N. Phan, and N. Shamsaei, "Powder Recycling Effects on the Tensile and Fatigue Behavior of Additively Manufactured Ti-6Al-4V Parts," JOM, vol. 71, no. 3, pp. 963–973, Mar. 2019, doi: 10.1007/s11837-018-3248-7.
- [24] A. Strondl, O. Lyckfeldt, H. Brodin, and U. Ackelid, "Characterization and Control of Powder Properties for Additive Manufacturing," *JOM*, vol. 67, no. 3, pp. 549–554, Mar. 2015, doi: 10.1007/s11837-015-1304-0.
- [25] A. Soltani-Tehrani, J. Pegues, and N. Shamsaei, "Fatigue Behavior of Additively Manufactured 17-4 PH Stainless Steel: The Effects of Part Location and Powder Re-use," *Additive Manufacturing*, Jun. 2020, doi: 10.1016/j.addma.2020.101398.
- [26] J. Clayton, D. Millington-Smith, and B. Armstrong, "The Application of Powder Rheology in Additive Manufacturing," JOM, vol. 67, no. 3, pp. 544–548, Mar. 2015, doi: 10.1007/s11837-015-1293-z.
- [27] Y. Murakami and S. Beretta, "Small Defects and Inhomogeneities in Fatigue Strength: Experiments, Models and Statistical Implications," Extremes, vol. 2, pp. 123–147, 1999, doi: 10.1023/A:1009976418553.
- [28] K. Gall, M. F. Horstemeyer, B. W. Degner, and J. Fan, "On the driving force for fatigue crack formation from inclusions and voids in a cast A356 aluminum alloy," *International Journal of Fracture*, vol. 108, pp. 207–233, 2001, doi: 10.1023/A:1011033304600.
- [29] P. H. Wirsching, "Fatigue reliability," *Prog. Struct. Engng. Mater.*, vol. 1, no. 2, pp. 200–206, Jan. 1998, doi: 10.1002/pse.2260010213.
- [30] P. H. Wirsching, "NASA Contractor Report 3697: Statistical Summaries of Fatigue Data for Design Purposes." NASA, Jul. 1983.
- [31] Y. Wu and P. H. Wirsching, "Advanced Reliability Method for Fatigue Analysis," *Journal of Engineering Mechanics*, vol. 110, no. 4, pp. 536–553, Apr. 1984, doi: 10.1061/(ASCE)0733-9399(1984)110:4(536).
- [32] A. Brot, "Weibull or Log-Normal Distribution to Characterize Fatigue Life Scatter Which Is More Suitable?," in ICAF 2019 Structural Integrity in the Age of Additive Manufacturing, A. Niepokolczycki and J. Komorowski, Eds. Cham: Springer International Publishing, 2020, pp. 551–561. doi: 10.1007/978-3-030-21503-3\_44.
- [33] W. Weibull, "A Statistical Distribution Function of Wide Applicability," ASME Journal of Applied Mechanics, pp. 293–297, Sep. 1951.
- [34] R. Sakin and İ. Ay, "Statistical analysis of bending fatigue life data using Weibull distribution in glass-fiber reinforced polyester composites," *Materials & Design*, vol. 29, no. 6, pp. 1170–1181, Jan. 2008, doi: 10.1016/j.matdes.2007.05.005.
- [35] M. Tiryakioğlu, "On the relationship between statistical distributions of defect size and fatigue life in 7050-T7451 thick plate and A356-T6 castings," *Materials Science and Engineering: A*, vol. 520, no. 1–2, pp. 114–120, Sep. 2009, doi: 10.1016/j.msea.2009.05.005.
- [36] M. Shirani and G. Härkegård, "Fatigue life distribution and size effect in ductile cast iron for wind turbine components," Engineering Failure Analysis, vol. 18, no. 1, pp. 12–24, Jan. 2011, doi: 10.1016/j.engfailanal.2010.07.001.
- [37] A. Altamura and D. Straub, "Reliability assessment of high cycle fatigue under variable amplitude loading: Review and solutions," Engineering Fracture Mechanics, vol. 121–122, pp. 40–66, May 2014, doi: 10.1016/j.engfracmech.2014.02.023.
- [38] E. Brandl, U. Heckenberger, V. Holzinger, and D. Buchbinder, "Additive manufactured AlSi10Mg samples using Selective Laser Melting (SLM): Microstructure, high cycle fatigue, and fracture behavior," *Materials & Design*, vol. 34, pp. 159–169, Feb. 2012, doi: 10.1016/j.matdes.2011.07.067.
- [39] K. S. Chan, M. Koike, R. L. Mason, and T. Okabe, "Fatigue Life of Titanium Alloys Fabricated by Additive Layer Manufacturing Techniques for Dental Implants," *Metall and Mat Trans A*, vol. 44, no. 2, pp. 1010–1022, Feb. 2013, doi: 10.1007/s11661-012-1470-4.
- [40] W. E. Luecke and J. A. Slotwinski, "Mechanical Properties of Austenitic Stainless Steel Made by Additive Manufacturing," J. RES. NATL. INST. STAN., vol. 119, p. 398, Oct. 2014, doi: 10.6028/jres.119.015.
- [41] G. Raugel and Y. Yi, "Recyclability Study on Inconel 718 and Ti-6Al-4V Powders for Use in Electron Beam Melting," *J Dyn Diff Equat*, vol. 27, no. 3–4, pp. 333–334, Dec. 2015, doi: 10.1007/s10884-015-9497-z.
- [42] L. C. Ardila et al., "Effect of IN718 Recycled Powder Reuse on Properties of Parts Manufactured by Means of Selective Laser Melting," Physics Procedia, vol. 56, pp. 99–107, 2014, doi: 10.1016/j.phpro.2014.08.152.
- [43] "Certificate of Analysis & Certificate of Conformity, TruForm 174-L62," Praxair Surface Technologies, Oct. 2018.
- [44] ASTM International, "E8/E8M-16ae1 Standard Test Methods for Tension Testing of Metallic Materials," ASTM International, West Conshohocken, PA, 2020.
- [45] ASTM International, "E466-15: Practice for Conducting Force Controlled Constant Amplitude Axial Fatigue Tests of Metallic Materials," ASTM International, West Conshohocken, PA, 2015. doi: 10.1520/E0466-15.

- [46] "AMS2759/3G Heat Treatment Precipitation-Hardening Corrosion-Resistant, Maraging, and Secondary Hardening Steel Parts," SAE International, 2018. doi: 10.4271/AMS2759/3H.
- [47] S. S. Wilks, "The Large-Sample Distribution of the Likelihood Ratio for Testing Composite Hypotheses," *Ann. Math. Statist.*, vol. 9, no. 1, pp. 60–62, Mar. 1938, doi: 10.1214/aoms/1177732360.
- [48] I. J. Myung, "Tutorial on maximum likelihood estimation," Journal of Mathematical Psychology, vol. 47, no. 1, pp. 90–100, Feb. 2003, doi: 10.1016/S0022-2496(02)00028-7.
- [49] R. Esmaeilizadeh, U. Ali, A. Keshavarzkermani, Y. Mahmoodkhani, E. Marzbanrad, and E. Toyserkani, "On the effect of spatter particles distribution on the quality of Hastelloy X parts made by laser powder-bed fusion additive manufacturing," *Journal of Manufacturing Processes*, vol. 37, pp. 11–20, Jan. 2019, doi: 10.1016/j.jmapro.2018.11.012.
- [50] Z. A. Young et al., "Types of spatter and their features and formation mechanisms in laser powder bed fusion additive manufacturing process," Additive Manufacturing, vol. 36, p. 101438, Dec. 2020, doi: 10.1016/j.addma.2020.101438.
- [51] L. E. Criales, Y. M. Arisoy, B. Lane, S. Moylan, A. Donmez, and T. Özel, "Laser powder bed fusion of nickel alloy 625: Experimental investigations of effects of process parameters on melt pool size and shape with spatter analysis," *International Journal of Machine Tools and Manufacture*, vol. 121, pp. 22–36, Oct. 2017, doi: 10.1016/j.ijmachtools.2017.03.004.
- [52] K. H. G. Chua and Y. Y. C. Choong, "Investigation of the effects on the print location during selective laser melting process," in *Proceedings of the 3rd International Conference on Progress in Additive Manufacturing*, 2018, pp. 613–618. doi: Proceedings of the 3rd International Conference on Progress in Additive Manufacturing.
- [53] J. H. Tan, W. L. E. Wong, and K. W. Dalgarno, "An overview of powder granulometry on feedstock and part performance in the selective laser melting process," *Additive Manufacturing*, vol. 18, pp. 228–255, Dec. 2017, doi: 10.1016/j.addma.2017.10.011.
- [54] ASTM International, "D7891-15 Standard Test Method for Shear Testing of Powders Using the Freeman Technology FT4 Powder Rheometer Shear Cell," ASTM International, West Conshohocken, PA, 2015.
- [55] H. K. Rafi, D. Pal, N. Patil, T. L. Starr, and B. E. Stucker, "Microstructure and Mechanical Behavior of 17-4 Precipitation Hardenable Steel Processed by Selective Laser Melting," J. of Materi Eng and Perform, vol. 23, no. 12, pp. 4421–4428, Dec. 2014, doi: 10.1007/s11665-014-1226-y.
- [56] B. AlMangour and J.-M. Yang, "Improving the surface quality and mechanical properties by shot-peening of 17-4 stainless steel fabricated by additive manufacturing," *Materials & Design*, vol. 110, pp. 914–924, Nov. 2016, doi: 10.1016/j.matdes.2016.08.037.
- [57] L. E. Murr et al., "Microstructures and Properties of 17-4 PH Stainless Steel Fabricated by Selective Laser Melting," Journal of Materials Research and Technology, vol. 1, no. 3, pp. 167–177, Oct. 2012, doi: 10.1016/S2238-7854(12)70029-7.
- [58] T. L. Starr, K. Rafi, B. Stucker, and C. M. Scherzer, "CONTROLLING PHASE COMPOSITION IN SELECTIVE LASER MELTED STAINLESS STEELS," in 23rd Annual International Solid Freeform Fabrication Symposium, Austin, Texas, 2012, p. 8.
- [59] P. D. Nezhadfar *et al.*, "Fatigue crack growth behavior of additively manufactured 17-4 PH stainless steel: Effects of build orientation and microstructure," *International Journal of Fatigue*, vol. 123, pp. 168–179, Jun. 2019, doi: 10.1016/j.ijfatigue.2019.02.015.
- [60] P. D. Nezhadfar, R. Shrestha, N. Phan, and N. Shamsaei, "Fatigue behavior of additively manufactured 17-4 PH stainless steel: Synergistic effects of surface roughness and heat treatment," *International Journal of Fatigue*, vol. 124, pp. 188–204, Jul. 2019, doi: 10.1016/j.ijfatigue.2019.02.039.
- [61] S. Romano, P. D. Nezhadfar, N. Shamsaei, M. Seifi, and S. Beretta, "High cycle fatigue behavior and life prediction for additively manufactured 17-4 PH stainless steel: Effect of sub-surface porosity and surface roughness," *Theoretical and Applied Fracture Mechanics*, vol. 106, Apr. 2020, doi: 10.1016/j.tafmec.2020.102477.
- [62] A. Yadollahi, M. Mahmoudi, A. Elwany, H. Doude, L. Bian, and J. C. Newman, "Fatigue-life prediction of additively manufactured material: Effects of heat treatment and build orientation," Fatigue Fract Eng Mater Struct, vol. 43, no. 4, pp. 831–844, Apr. 2020, doi: 10.1111/ffe.13200.
- [63] J. Schijve, Fatigue of structures and materials, Second edition. Dordrecht: Springer, 2009.
- P. D. Nezhadfar, K. Anderson-Wedge, S. R. Daniewicz, N. Phan, S. Shao, and N. Shamsaei, "Improved high cycle fatigue performance of additively manufactured 17-4 PH stainless steel via in-process refining micro-/defect-structure," *Additive Manufacturing*, vol. 36, p. 101604, Dec. 2020, doi: 10.1016/j.addma.2020.101604.